

5-21-2019

Pt nanoparticles decorated heterostructured g-C₃N₄/Bi₂MoO₆ microplates with highly enhanced photocatalytic activities under visible light

Z. Jia

F. Lyu

Laichang Zhang
Edith Cowan University

S. Zeng

Shunxing Liang
Edith Cowan University

See next page for additional authors

Follow this and additional works at: <https://ro.ecu.edu.au/ecuworkspost2013>



Part of the [Engineering Commons](#)

10.1038/s41598-019-42973-6

Jia, Z., Lyu, F., Zhang, L., Zeng, S., Liang, S., Li, Y. Y., & Lu, J. (2019). Pt nanoparticles decorated heterostructured gC₃N₄/Bi₂MoO₆ microplates with highly enhanced photocatalytic activities under visible light. *Scientific Reports*, 9(1), Article 7636. Available [here](#)

This Journal Article is posted at Research Online.
<https://ro.ecu.edu.au/ecuworkspost2013/6200>


Authors

Z. Jia, F. Lyu, Laichang Zhang, S. Zeng, Shunxing Liang, Y. Y. Li, and J. Lu

SCIENTIFIC REPORTS

OPEN

Pt nanoparticles decorated heterostructured g-C₃N₄/Bi₂MoO₆ microplates with highly enhanced photocatalytic activities under visible light

Z. Jia^{1,2}, F. Lyu^{1,2}, L. C. Zhang³, S. Zeng^{4,5}, S. X. Liang³, Y. Y. Li^{4,5,6} & J. Lu^{1,2,6} 

Exploring an efficient and photostable heterostructured photocatalyst is a pivotal scientific topic for worldwide energy and environmental concerns. Herein, we reported that Pt decorated g-C₃N₄/Bi₂MoO₆ heterostructured composites with enhanced photocatalytic performance under visible light were simply synthesized by one-step hydrothermal method for methylene blue (MB) dye degradation. Results revealed that the synthetic Pt decorated g-C₃N₄/Bi₂MoO₆ composites with Bi₂MoO₆ contents of 20 wt.% (Pt@CN/20%BMO) presented the highest photocatalytic activity, exhibiting 7 and 18 times higher reactivity than the pure g-C₃N₄ and Bi₂MoO₆, respectively. Structural analyses showed that Bi₂MoO₆ microplates were anchored on the wrinkled flower-like g-C₃N₄ matrix with Pt decoration, leading to a large expansion of specific surface area from 10.79 m²/g for pure Bi₂MoO₆ to 46.09 m²/g for Pt@CN/20%BMO. In addition, the Pt@CN/20%BMO composites exhibited an improved absorption ability in the visible light region, presenting a promoted photocatalytic MB degradation. Quenching experiments were also conducted to provide solid evidences for the production of hydroxyl radicals ([•]OH), electrons (e⁻), holes (h⁺) and superoxide radicals ([•]O₂⁻) during dye degradation. The findings in this critical work provide insights into the synthesis of heterostructured photocatalysts with the optimization of band gaps, light response and photocatalytic performance in wastewater remediation.

Advanced oxidation processes (AOPs) with their superior purification efficiency of toxic organic compounds have been recently attracted large attentions in industrial wastewater treatment^{1–6}. Compared to alternatives, such as Fenton/Fenton-like process^{7–9} and ozone oxidation^{10–12}, semiconductor photocatalysts have received tremendous attentions to address the worldwide environmental and energy concerns¹³. Since Fujishima and Honda discovered the photoelectrochemical effects of TiO₂¹⁴, the research of various single component semiconductors, such as oxides^{15,16} and sulfide semiconductors^{17,18}, has caught much attentions in the last decades. However, many reports have demonstrated that these single component semiconductors are photo-instability, fast recombination rate of electron hole pairs and wide band gaps¹⁹, exhibiting a significant limitation in achieving practical industrialization. To date, attempts have been made to overcome these disadvantages. For example, doping agents with non-metal ions, metalloids or ionic groups on the photocatalysts could effectively alter energy band structure and carrier separation²⁰. It was found that N-doped CeO_x nanoparticles on g-C₃N₄ matrix presented a promoted photocatalytic activity due to formation of intimate interfacial contact²¹. B-doped BiOBr nanosheets could enhance the charge carrier separation efficiency, thereby enhancing the ability of accepting electrons from the valence

¹Hong Kong Branch of National Precious Metals Material Engineering Research Center, Department of Material Science and Engineering, City University of Hong Kong, Hong Kong, China. ²Department of Mechanical Engineering, City University of Hong Kong, Hong Kong, China. ³School of Engineering, Edith Cowan University, 270 Joondalup Drive, Joondalup, Perth, WA, 6027, Australia. ⁴Center of Super-Diamond and Advanced Films (COSDAF), City University of Hong Kong, Kowloon, Hong Kong, China. ⁵Department of Physics and Materials Science, City University of Hong Kong, Kowloon, Hong Kong, China. ⁶Centre for Advanced Structural Materials, City University of Hong Kong, Shenzhen Research Institute, 8 Yuexing 1st Road, Shenzhen Hi-Tech Industrial Park, Nanshan District, Shenzhen, China. Correspondence and requests for materials should be addressed to J.L. (email: jianlu@cityu.edu.hk)

band of BiOBr²². PO₄ ionic group doped Bi₂WO₆ nanoplates demonstrated a significant regulation of their band structure, charge carrier separation efficiency and light absorbance for improving photocatalytic activity²⁰. In addition, synthesis of heterojunction structure²³ and decoration of noble metals²⁴ in photocatalysts with enhanced visible light response and easy separation of electron-hole pairs have also induced extensive interests in recent years. For example, the formation of heterojunction structure on TiO₂²⁵, ZnO²⁶ and some carbon matrix such as g-C₃N₄²⁷, r-GO²⁸ and carbon nanotubes²⁹ presents an efficient separation of electrons and holes to facilitate photocatalytic activity. The decoration of noble metals, such as Au³⁰, Ag³¹, Pt³² and Pd³³ exhibits an improved light response to extend the light absorbance range.

Bi₂MoO₆, as one of the most important members in Aurivillius oxide family, is always at the cutting edge of research in photocatalytic degradation of organic pollutions³⁴ and energy evolution³⁵. The pure Bi₂MoO₆ with a relatively lower band gap (2.5–2.8 eV)³⁶ presents an enhanced light response compared to some photocatalytic stars, such as TiO₂ and ZnO with the band gaps of 3.2–3.3 eV³⁷. However, due to their fast recombination efficiency of charge carriers, Bi₂MoO₆ usually presents a poor quantum yield that would greatly restrain their practical applications. So far, many attempts have been exploited to improve the photocatalytic performance of Bi₂MoO₆, such as doping lanthanide ions³⁸ or noble metals³⁹ to act as redox centers, the formation of heterojunction structures containing metal oxides⁴⁰, metal sulfates⁴¹ or carbon materials⁴², etc.

Recently, g-C₃N₄ with its superior optical properties (band gap \approx 2.7 eV) and photostability has been widely employed as a matrix to synthesize heterostructured photocatalysts⁴³. The unique structure of covalently-linked sp² bonded carbon network with the decoration of nitrogen atoms in g-C₃N₄ presents an excellent thermal and chemical stability. Moreover, the large scaffold structure could undoubtedly provide a large specific surface area for being anchored by other semiconductors and also could effectively prevent the particle aggregation. Nevertheless, the most important drawback of high recombination rate for the electron-hole pairs still largely inhibits their extensive applications. As such, the formation of heterojunctions by two semiconductors or anchoring noble metallic nanoparticles is rapid development in recent years, for example, the synthesis of g-C₃N₄ with semiconductors of TiO₂⁴⁴, ZnO⁴⁵, NaNbO₃⁴⁶, Bi₂WO₆⁴⁷ or TaON⁴⁸ and the decoration of noble metals on g-C₃N₄ by Au⁴⁹, Pt⁵⁰, Ag⁵¹ or Pd⁵². However, the current studies have been focusing on synthesizing photocatalysts with two components. There are few attempts to investigate the noble metals being anchored on the heterojunctions, in which the optical structure is regulated by the synthesis of two semiconductors with a similar band gap and the electron-hole recombination efficiency is effectively suppressed by the noble metals doping.

In this work, Pt decorated g-C₃N₄/Bi₂MoO₆ heterostructured semiconductors are synthesized by one-step hydrothermal method to investigate their photocatalytic activity of MB degradation under visible light. Various amounts of Bi₂MoO₆ loading (10%, 20% and 50%) on g-C₃N₄ matrix are initially examined to demonstrate the optimal combination of the two semiconductors followed by Pt decoration. The structures of the synthetic composites are systematically characterized. The MB degradation and mineralization as well as the corresponding reaction kinetics (k_{obs}) using the synthetic photocatalysts are comparatively investigated in detail. Quenching experiments by adding radical scavengers are also conducted to study the photocatalytic mechanisms.

Results

Structures and morphologies. Figure 1 shows scanning electron microscope (SEM) images of the as-prepared g-C₃N₄ (CN), Bi₂MoO₆ (BMO), g-C₃N₄/Bi₂MoO₆ composites with Bi₂MoO₆ contents of 10 wt.% (CN/10%BMO), of 20 wt.% (CN/20%BMO), of 50 wt.% (CN/50%BMO) and Pt decoration (Pt@CN/20%BMO), providing a direct view of surface morphologies of the photocatalysts. As shown in Fig. 1a, the obtained pure CN presents a flower-like structure with multiple wrinkled-layers, exhibiting a large surface area for further BMO and Pt nanoparticles decoration. Fig. 1b presents the pure BMO microplates with a laminar and irregular sheet-like microstructure. Notably, the BMO microplates have much smaller particle size than the CN, demonstrating great potential for them to anchor on the CN matrix. Fig. 1c–e show the morphologies of BMO and CN composites with a certain amount of BMO loading of 10%, 20% and 50%, respectively. Apparently, a denser BMO laminar sheet (Fig. 1d,e) is decorated on the wrinkled CN matrix compared to the CN/10%BMO loading in Fig. 1c. In addition, the size of the anchored BMO (Fig. 1c–e) is much smaller than that of the pure BMO (Fig. 1b) without altering the sheets-like morphology, providing more active sites for dye degradation. The smaller size of the anchored BMO is primarily ascribed to the initial adsorption of Bi³⁺ onto the CN according to the benefit of facile one-step hydrothermal synthetic method. The morphology of Pt@CN/20%BMO composites and atomic mapping images, e.g., Bi, Mo, C for CN/20%BMO and Pt, Bi, C for Pt@CN/20%BMO, are shown in Fig. 1f–h, providing a solid indication for the formation of Pt@CN/20%BMO heterojunctions.

Figure 2 shows transmission electron microscopy (TEM) and high resolution TEM (HRTEM) images of CN, CN/10%BMO, CN/20%BMO, CN/50%BMO and Pt@CN/20%BMO. The pure CN presents a wrinkled and layered morphology, as shown in Fig. 2a, which agrees with the SEM image (Fig. 1a) and other reports⁵³. Fig. 2b–d imply the formation of CN and BMO heterojunctions and further reveal that the anchored BMO is in a sheet-like microplate. HRTEM images of CN/20%BMO and Pt@CN/20%BMO are presented in Fig. 2e,f. A lattice fringe with a space of 0.32 nm (Fig. 2e) corresponds to (131) plane of BMO, while the spacing of 0.22 nm (Fig. 2f) is ascribed to (111) plane of Pt with a particle size of \sim 5 nm. The fast fourier transform (FFT) images in the insets of Fig. 2e,f show that the single-crystalline structure of BMO is converted to poly-crystalline structure of Pt and BMO composites. Combining the elemental mapping images in Fig. 2g, this result further confirms the successful formation of Pt@CN/20%BMO heterojunctions.

The crystalline structures of the as-prepared samples are also investigated by X-ray diffraction (XRD) (Fig. 3). Two distinct peaks at 13.1° and 27.3° are observed on the CN curve, indicating (100) plane of tri-s-triazine group and (002) plane of aromatic laminar sheets, respectively⁵⁴. XRD patterns are clearly characterized to confirm the orthorhombic crystalline structure of γ -BMO (JCPDS No. 21-0102)⁴⁰. The strongest intensity at (131) plane is in accordance with the result of HRTEM image (Fig. 2c). For the CN/BMO composites, all the characterized

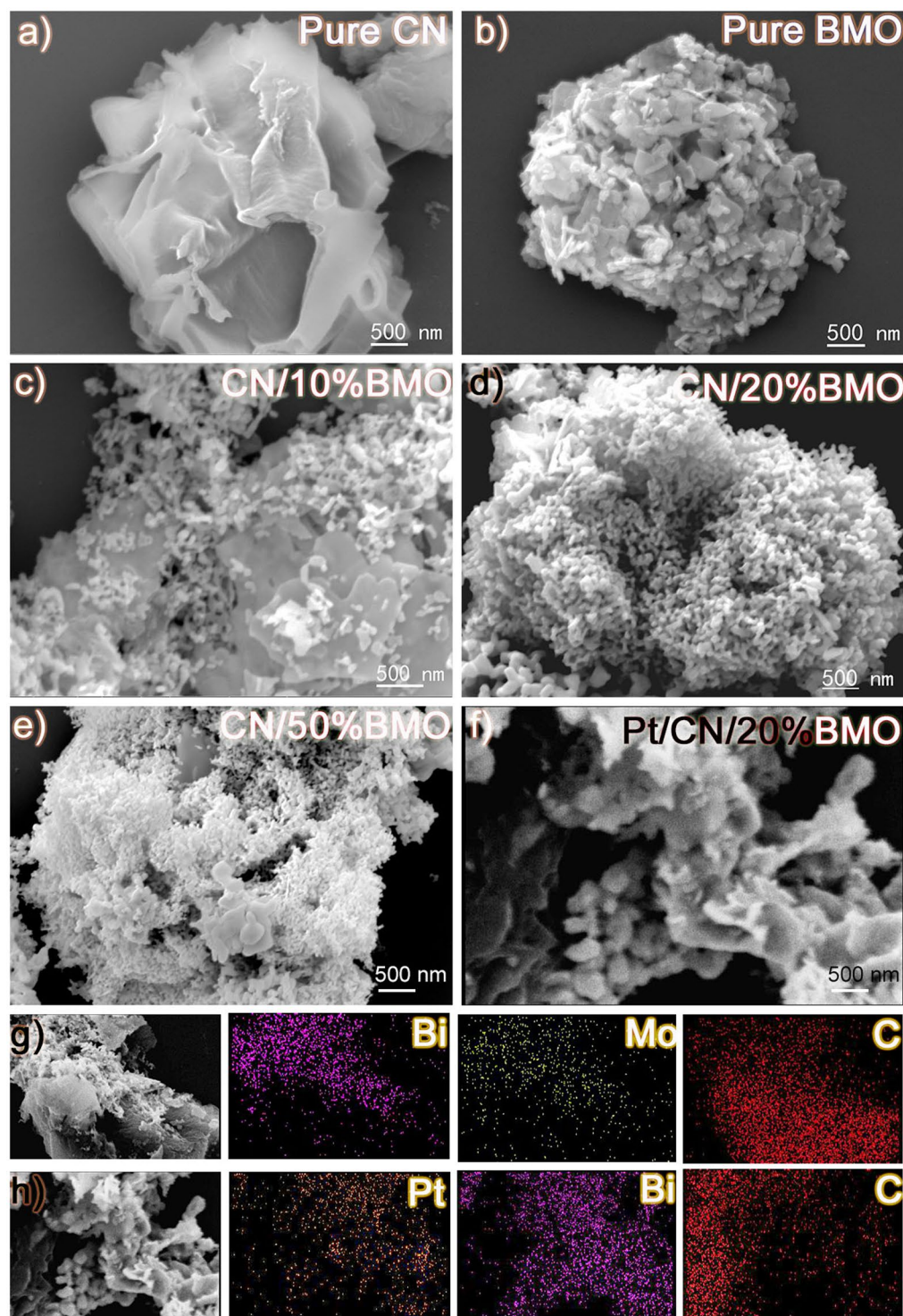


Figure 1. SEM images of (a) CN, (b) BMO, (c) CN/10%BMO, (d) CN/20%BMO, (e) CN/50%BMO, (f) Pt@CN/20%BMO and corresponding elemental mapping results of (g) CN/20%BMO and (h) Pt@CN/20%BMO.

diffraction peaks of BMO are remained, demonstrating the successful formation of heterojunctions. However, the peaks at (100) and (002) plane of CN are detected to be invisible and be overlapped with the peak at (131) plane of BMO, which is similar to other report⁵⁵. For the Pt@CN/20%BMO composites, characterized diffraction peaks of Pt at 40.1, 46.9 and 67.9° indicate the (111), (100) and (220) planes while all the peaks of BMO are clearly observed, demonstrating Pt nanoparticles are decorated on the CN/BMO heterojunctions.

Chemical states. X-ray photoelectron spectroscopy (XPS) and fourier-transform infrared spectroscopy (FTIR) analyses have been conducted to confirm the surface chemical and valence states of the as-prepared

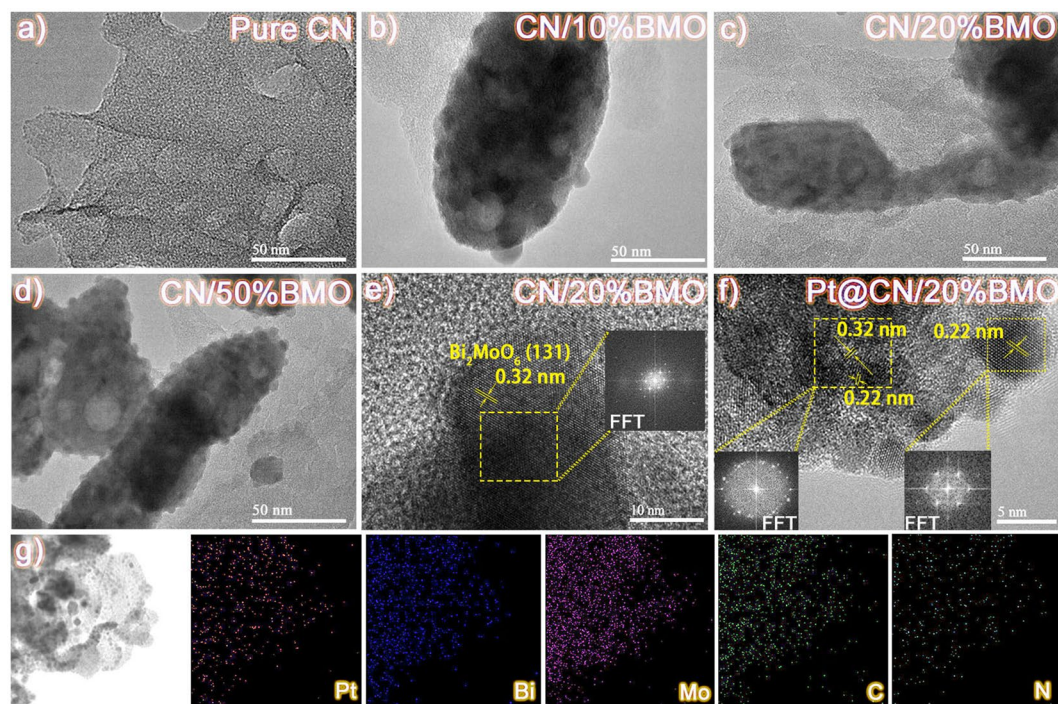


Figure 2. TEM images of (a) CN, (b) CN/10%BMO, (c) CN/20%BMO, (d) CN/50%BMO and HRTEM images of (e) CN/20%BMO, (f) Pt@CN/20%BMO (insets are FFT images of the selected areas) as well as the corresponding elemental mapping results of (g) Pt@CN/20%BMO.

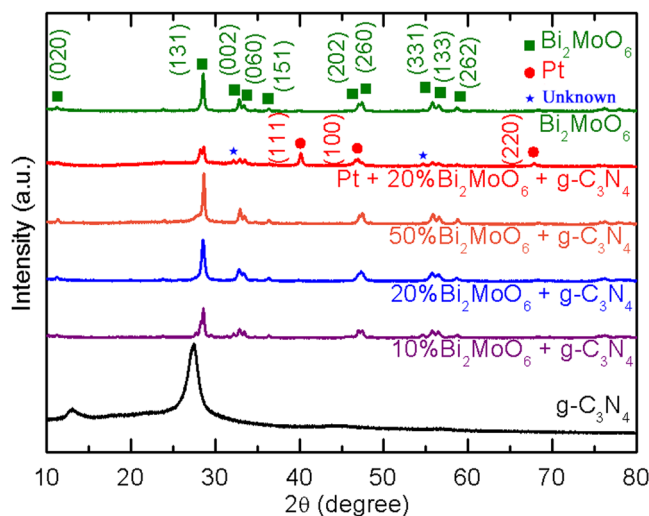


Figure 3. XRD characterization of the as-prepared photocatalysts.

samples. As shown in Figure S1, the elements including Pt, Bi, Mo, O, C and N with strong intensities are observed in the composites. No other impurity peaks are obtained. Fig. 4a shows the high-resolution spectra of Bi 4f spectra for BMO, CN/20%BMO and Pt@CN/20%BMO. The bonding energies at 159.1 and 164.4 eV correspond to Bi 4f_{7/2} and Bi 4f_{5/2} of Bi³⁺, respectively⁵⁶. For the Mo 3d spectra in Fig. 4b, the peaks located at 232.3 and 235.5 eV are attributed to Mo 3d_{3/2} and Mo 3d_{5/2} of Mo⁶⁺, respectively. In the O 1s spectra (Fig. 4c), it is noted that the peak at 530.0 eV of pure BMO presents slight shifts to 529.9 eV and 530.1 eV for CN/20%BMO and Pt@CN/20%BMO samples, respectively. The shifted peaks in Bi 4f and Mo 3d (Fig. 4a,b) indicate formation of the groups of Bi-O and Mo-O⁵⁷. Such results further imply the formation of CN/BMO heterojunctions with Pt decoration. Fig. 4d shows the high resolution of Pt 4f spectra. The characterized peaks at 70.9 and 74.2 eV of Pt⁰ are clearly observed on 4f_{7/2} and 4f_{5/2}, respectively. The peaks at 72.0 and 75.6 eV are attributed to Pt²⁺, indicating the formation of Pt-O⁵⁸ and further demonstrating the partial pre-adsorption of Pt²⁺ onto the CN matrix during the facile one-step hydrothermal synthetic method. Fig. 5 shows the FTIR results of the as-prepared composites. For the pure CN, a group of characterized peaks are clearly observed in the range from 1241 to 1639 cm⁻¹. In detail,

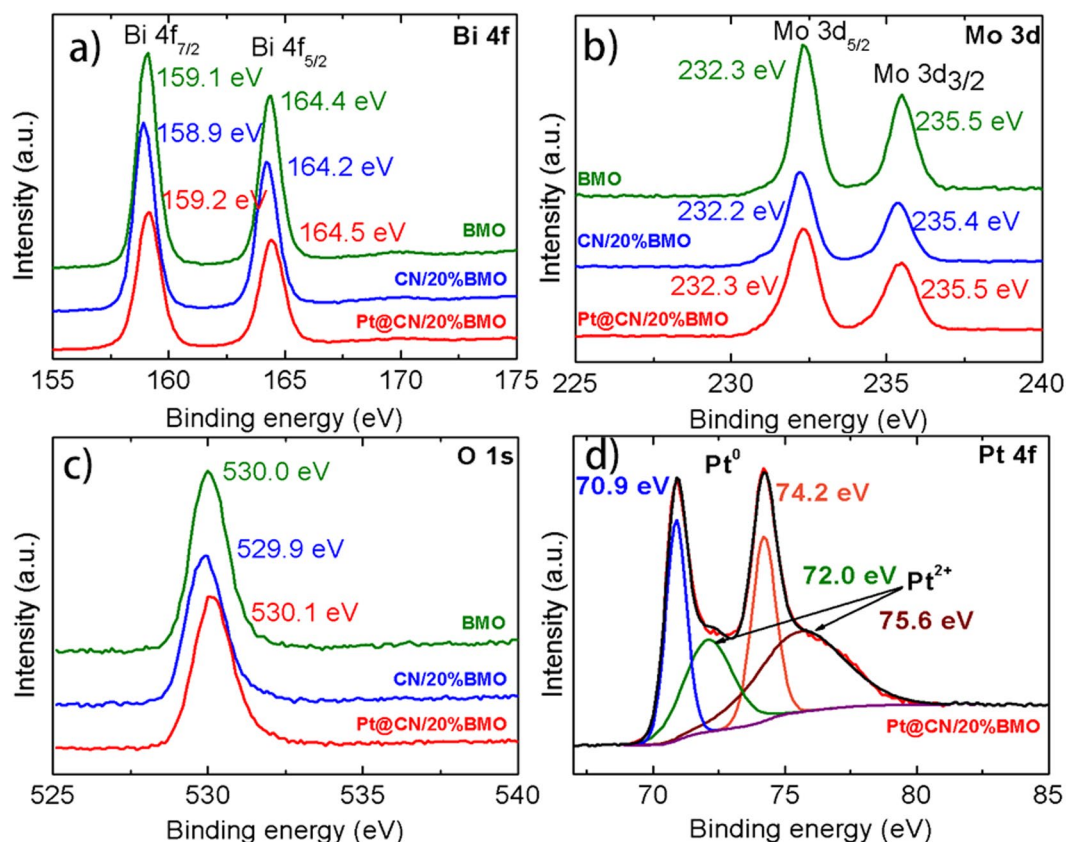


Figure 4. XPS results of the as-prepared photocatalysts: high-resolution spectra of (a) Bi 4f, (b) Mo 3d, (c) O 1s and (d) Pt 4f.

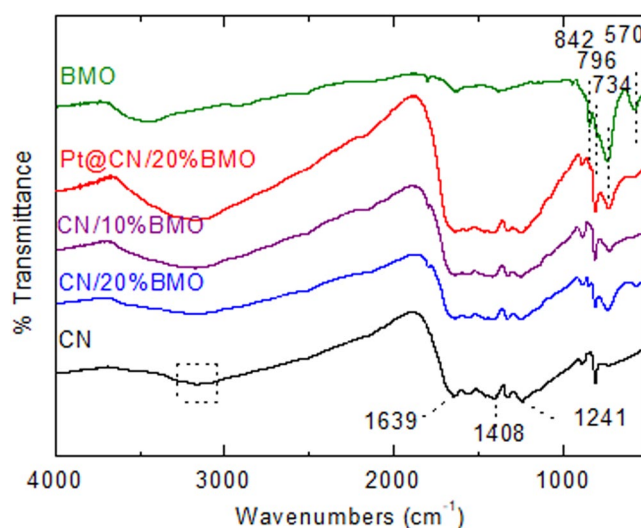


Figure 5. FTIR spectra of the as-prepared photocatalysts.

the peaks located at 1241, 1325 and 1408 cm^{-1} are attributed to the stretching vibration mode of C-N bonds with the aromatic structure, while the peak at 1639 cm^{-1} can be ascribed to the stretching vibration mode of $\text{C}\equiv\text{N}$ ⁵⁹. For the pure BMO, the characterized peaks located at 570 and 734 cm^{-1} indicate the bending vibration of the octahedral structure and the asymmetric stretching mode in MoO_6 , respectively, while the wavenumbers at 796 and 842 cm^{-1} correspond to the Mo-O symmetric and asymmetric stretching vibration modes in the MoO_6 octahedral structure⁵⁹. Clearly, all the characterized peaks in pure CN and BMO are presented in the CN/20%BMO and Pt@CN/20%BMO composites, demonstrating the successful formation of the photocatalysts. Such a result is in great agreement with the aforementioned SEM, TEM and XRD analyses.

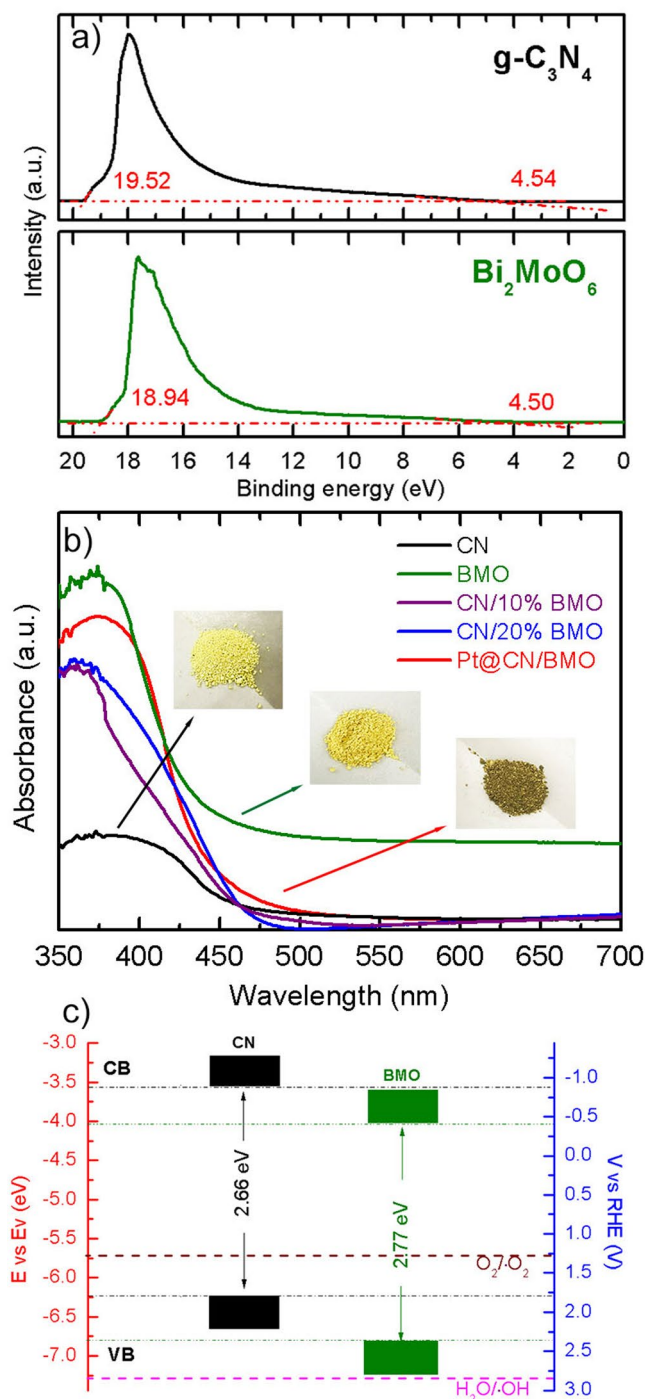


Figure 6. (a) UPS spectra, (b) UV-Vis DRS spectra, and (c) the estimated band gap structures of the CN and BMO.

Optical property. The optical property plays a significant role in revealing the band gap structures of heterojunction photocatalysts. Fig. 6a shows the ultraviolet photoelectron spectroscopy (UPS) spectra of the as-prepared CN and BMO composites to indicate the Fermi (E_{Fermi}) and cut-off ($E_{\text{cut-off}}$) energy states by estimating the intersection values. Notably, the valence band energy (E_{VB}), which is equivalent to the ionization potential (φ), is calculated by the equation below (Equation 1)⁵⁴:

$$\varphi = h\nu - E_{\text{cut-off}} + E_{\text{Fermi}} \quad (1)$$

whereas $h\nu$ is the photon energy from He I source as 21.22 eV.

The values of φ are then calculated as 6.24 and 6.78 eV for the as-prepared CN and BMO, respectively, suggesting the electrons would transfer from CN to BMO ($\varphi_{\text{CN}} < \varphi_{\text{BMO}}$) after the formation of heterojunction structure⁴⁰.

In order to find out the position of conduction band (E_{CB}), the band gap energy (E_g) is estimated by UV-Vis diffuse reflectance spectrum (UV-DRS) spectra as shown in Fig. 6b using the equation below (Equation 2)⁶⁰,

$$E_g(\text{eV}) = 1240/\lambda_g \quad (2)$$

whereas the absorption edge (λ_g) is observed by the intersection values of the tangent and the wavelength axis.

The values of E_g and E_{CB} of the as-prepared CN and BMO samples can be subsequently calculated as 2.66, 2.77 eV (E_g) and 3.58, 4.01 eV ($E_{CB} = E_{VB} - E_g$), respectively. In the expression of reversible hydrogen electrode (RHE) vs. volts (V) (0 V in RHE is equivalent to -4.44 eV in energy potential⁶¹), the E_{CB} can be positioned at -0.86 and -0.43 V of the CN and BMO composites, respectively. Fig. 6c presents the estimated band structures of the prepared CN and BMO samples according to the above calculation. Due to the similar band structures of CN and BMO, the electrons in the CB and the holes in the VB would be promoted from the CN to BMO and BMO to CN, respectively. The electronic motion in the modified band structure of CN/BMO heterostructures would be improved, and more importantly, the inclusion of Pt nanoparticles as electron mediators anchoring on the CN/BMO heterostructures would further promote the electron transfer. In addition, the observation of the improved absorption intensity in the visible light region for the Pt@CN/20%BMO photocatalyst indicates that the band structure could be effectively altered to enhance the visible light response and charge transformation. The improved absorption intensity and slight red shift of Pt@CN/20%BMO photocatalyst can be ascribed to the localized surface plasmon resonances (LSPRs) of Pt nanoparticles²⁴, which would enhance the photocatalytic activity for dye degradation.

The heterogeneous photocatalytic activity is also significantly influenced by the specific surface area of photocatalysts due to the provision of surface-reactive sites. Figure S2 presents the nitrogen adsorption/desorption isotherms of the as-prepared samples. Clearly, strong N_2 adsorption/desorption curves are observed in the pressure range of 0.1–0.9, indicating the capillary condensation in large mesopores exists in all the samples⁵⁵. As shown in Figure S2 inset, the Brunauer-Emmett-Teller (BET) specific surface area of Pt@CN/20%BMO with $46.09 \text{ m}^2/\text{g}$ presents significant improvement compared to the pure BMO with $10.79 \text{ m}^2/\text{g}$ and CN/20%BMO with $39.92 \text{ m}^2/\text{g}$, respectively. In addition, the Pt@CN/20%BMO with a total pore volume of $1.092 \text{ cm}^3/\text{g}$ (Barrett-Joyner-Halenda (BJH) process) would provide much more active sites compared to the other samples. Such results are in accordance with the above SEM analysis. The Pt nanoparticles and BMO laminar sheets are densely distributed on the wrinkled CN matrix that would lead to a higher photocatalytic activity for the following dye degradation. Figure S3 shows the thermogravimetric analysis (TGA) results of the as-prepared samples. It is noted that the TGA curve of the pure CN presents a sharp weight loss in the temperature range from 500 to 680°C and nearly no CN remaining after 680°C , while there is only 1.1% weight loss for the pure BMO samples due to the slight adsorption and activation of atmospheric oxygen⁵⁵. However, the significant weight loss of CN/20%BMO and Pt@CN/20%BMO is shifted to the temperature range from 400 to 580°C and 380 to 570°C , respectively. Surprisingly, the obtained ratio between BMO and CN from TGA result is higher than the theoretical value of 20%, which is mainly attributed to the existence of BMO and Pt would promote the oxidation of CN and the adsorption of atmospheric oxygen. Similar performance has been reported in $\text{g-C}_3\text{N}_4/\text{Bi}_2\text{MoO}_6$ ⁵⁵ and $\text{g-C}_3\text{N}_4/\text{SmVO}_4$ ⁶² heterojunction photocatalysts.

Photocatalytic activity. The photocatalytic activity of the as-prepared samples was examined by the degradation of MB dye under visible light ($\lambda \geq 420 \text{ nm}$). As shown in Fig. 7a, the MB dye without the addition of catalysts presents negligible change under visible light irradiation even for 150 min. However, when adding the synthetic CN/BMO composites, the MB degradation efficiency has a significant increase compared to the pure BMO or CN, demonstrating the superior photocatalytic activity of the as-prepared heterojunction structures. In order to find out the optimal weight percentage of BMO, the CN/BMO composites with BMO loading of 10%, 20% and 50% are investigated for the MB degradation. It is interesting that the photocatalytic activity is remarkably improved when increasing the BMO contents from 0% to 20%, while 90% of MB degradation for CN/20%BMO compared with only 38% of MB degradation for the pure BMO at 150 min. However, when 50% of BMO is loaded, the MB degradation presents a significant decrease to be even lower than the pure CN. It is owing to the excessive BMO microplates could cover the surface of CN so that to reduce the photon adsorption in the synthetic heterostructural CN/BMO photocatalysts, and moreover, the formation of heterojunction could be suppressed by the inclusion of excessive BMO microplates due to self-agglomerate phenomenon⁶³, which is in good accordance with the SEM image in Fig. 1e. Such performance suggests that the CN/BMO composite with 20% BMO loading exhibits the optimal photocatalytic activity for dye degradation. On this basis, further study is investigated for the Pt@CN/20%BMO composites. Clearly, the Pt decorated photocatalysts present a significant enhancement for the MB degradation compared to all the others, whereas nearly 100% dye degradation is achieved at 120 min, indicating that its heterojunction structure is successfully regulated by the facile hydrothermal synthesis. The corresponding kinetic rates (k_{obs}) of the as-prepared samples for MB degradation are calculated by the pseudo-first-order kinetics model (Equation 3) as shown in Fig. 7b.

$$\ln(C_0/C) = k_{obs}t \quad (3)$$

whereas k_{obs} is the kinetic rate constant; C_0 is the original concentration of dye; C is the dye concentration at time t .

Notably, the Pt@CN/20%BMO composites with the $k_{obs} = 0.036 \text{ min}^{-1}$ presents 7 times and 18 times higher photocatalytic activity than the pure CN with $k_{obs} = 0.005 \text{ min}^{-1}$ and BMO with $k_{obs} = 0.002 \text{ min}^{-1}$, respectively. In addition, the photoactivity of the synthetic Pt@CN/20%BMO composites is much promoted than the commercial p-25 with $k_{obs} = 0.002 \text{ min}^{-1}$ and also other state-of-the-art ternary photocatalysts under visible light (Table 1), demonstrating their excellent catalytic property in wastewater remediation. Fig. 7c presents the UV-Vis spectra

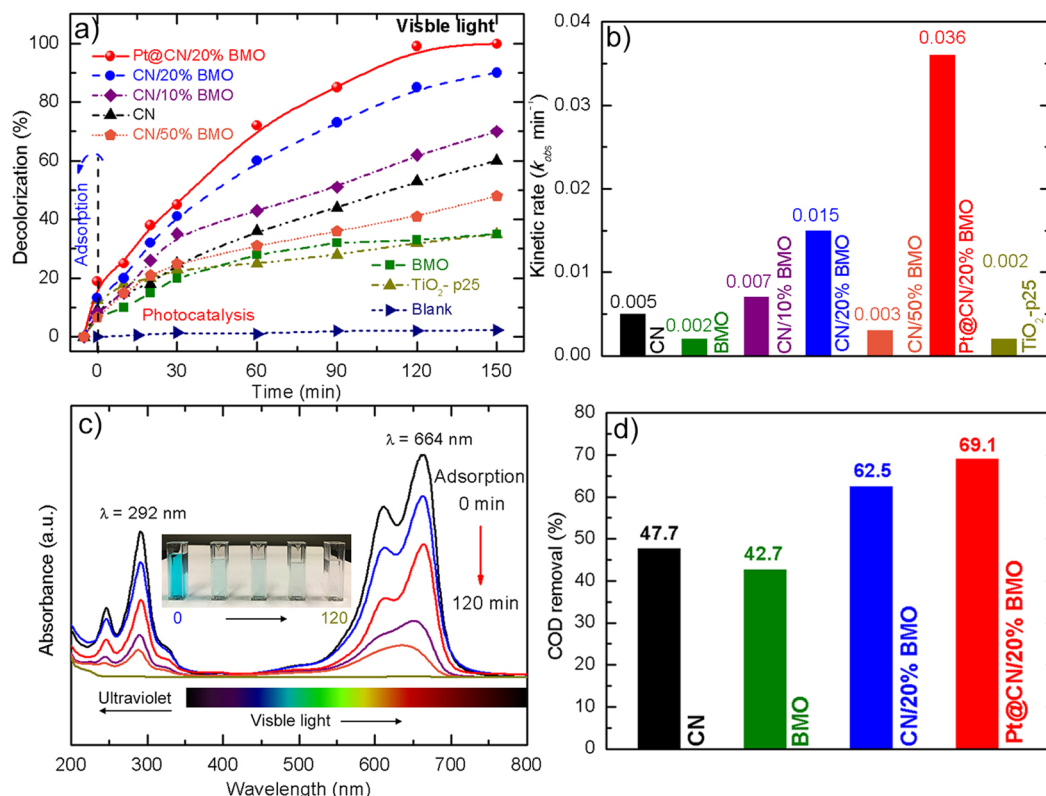


Figure 7. (a) photocatalytic MB degradation and (b) corresponding kinetic rates (k_{obs}) of the as-prepared samples, (c) UV-Vis spectra of color removals for Pt@CN/20%BMO photocatalysts and (d) COD removals at 150 min of as-prepared samples under visible light.

SC 1	SC 2	Metallic mediators	Light source (Power, W)	Organic pollutants	Degradation (%) and Time (h)	Ref.
CdS	TiO ₂	Au	LP Hg lamp (20)	MB	72 and 2	70
g-C ₃ N ₄	BiPO ₄	Au	Xe lamp (300)	MO	88 and 2.66	71
MoS ₂	Ag ₃ PO ₄	Ag	Solar Xe arc lamp (35)	PhOH	95 and 2	72
g-C ₃ N ₄	WO ₃	Cu, Ag, Au	Xe arc lamp (500)	4-NPhOH	100 and 2	73
In ₂ S ₃	Ag ₂ CrO ₄	Ag	Xe arc lamp (300)	MO	65.3 and 2	74
ZnS	Ag ₃ PO ₄	Ag	Xe lamp (350)	MB	82 and 2	75
g-C ₃ N ₄	Ag ₂ CrO ₄	Ag	HP Xe Lamp (500 W)	2,4-DCP	94 and 2	76
CdS	BiOCl	Au	Xe lamp (300)	SD	100 and 4	77
g-C ₃ N ₄	Bi ₂ MoO ₆	CNT	Xe lamp (500)	2,4-DBP	68.8 and 2	78
g-C ₃ N ₄	Bi ₂ MoO ₆	Pt	Xe lamp (300)	MB	100 and 2	This work

Table 1. Comparison of ternary photocatalysts for degradation of organic pollutants under visible light.

of MB degradation using 0.5 g/L of Pt@CN/20%BMO photocatalyst at different time intervals. It can be observed that the characterized peaks at $\lambda = 292$ nm (triazine group) and $\lambda = 664$ nm (heteropoly aromatic linkage) of MB gradually decrease to be invisible from 0 min to 120 min, indicating the organic components in the dye are decomposed to nontoxic NO_3^- , SO_4^{2-} , H_2O and CO_2 ^{3,64}. The slight blue shift (towards blue end in the spectrum) of the absorbance in MB dye from 664 nm to 634 nm is likely ascribed to the initial degradation of auxochrome ($-\text{CH}_3$), resulting in a slight color change during photocatalytic activity⁶⁵. The inset of Fig. 7c presents a solid evidence of the visible color change during MB degradation.

Fig. 7d shows the chemical oxygen demand (COD) removals of the as-prepared samples at 150 min under visible light irradiation. Notably, the pure CN and BMO with the COD removals of 47.7% and 42.7% present a relatively poor performance compared with the Pt@CN/20%BMO composites with the COD removal of 69.1%, further implying the synthetic Pt@CN/20%BMO photocatalyst can effectively mineralize the MB dye into H_2O and CO_2 during the photocatalytic performance. Such a result is in good accordance with the above analyses of the promoted regulation of electron transfer, specific surface area and surface morphology, etc.

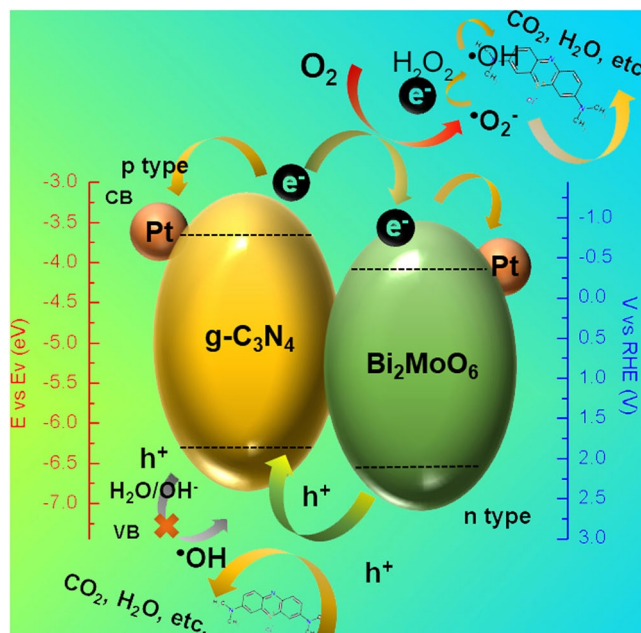


Figure 8. Schematic graph of the proposed photocatalytic mechanism for the synthetic Pt decorated CN/BMO heterojunctions.

It is well accepted that the progress of dye molecule decomposition is mainly due to the generation of the active species during photocatalysis. To identify these dominant active species, various radical scavengers including IPA, CrO_3 , SO and BQ are employed to prove the generation of $\bullet\text{OH}$, e^- , h^+ and $\bullet\text{O}_2^-$, respectively^{35,59,66}. As shown in Figure. S4, the addition of IPA causes a decrease in MB degradation compared to the only addition of Pt@CN/20%BMO photocatalysts, suggesting the $\bullet\text{OH}$ radicals are gradually formed during this photocatalytic activity. In comparison, the MB degradation efficiency is more affected by the addition of CrO_3 , SO and BQ, leading to the efficiency sharply decreases to nearly 50% at 150 min. Such performance indicates that the generated e^- , h^+ and $\bullet\text{O}_2^-$ are the dominant oxidants for MB degradation in this work.

Discussion

Fig. 8 shows the proposed photocatalytic mechanism of the synthetic heterojunctions. Considering the above band gap analysis in Fig. 6, the photo-induced h^+ with an energy of 2.34 V at VB presents lower energy state than the $\bullet\text{OH}$ of 2.70 V, leading to the $\bullet\text{OH}$ cannot be directly activated from H_2O during the photocatalysis. The existing $\bullet\text{OH}$ is produced by the reaction of e^- and the gradually generated H_2O_2 ⁵⁹. This is the reason why sole $\bullet\text{OH}$ plays partially synergistic dye degradation in this work. Therefore, the h^+ with strong oxidation ability is directly employed for decomposing the MB molecule. In comparison, the potential of e^- with the value of -0.86 V at CB is much negative than the $\bullet\text{O}_2^-$ with the value of 1.23 V, resulting in easy reduction of dissolved O_2 to $\bullet\text{O}_2^-$ thereby degrading the organic matters. More importantly, the decorated Pt nanoparticles in this work play a significant role to serve as a solid-state electron mediator. The generated e^- on the CB of $\text{g-C}_3\text{N}_4$ in the heterojunctions is easily transferred to the Pt particles and Bi_2MoO_6 microplates that would effectively promote electron transfer and suppress the electron-hole recombination efficiency⁵⁵. In addition, the produced h^+ also could migrate from Bi_2MoO_6 to $\text{g-C}_3\text{N}_4$ in the heterojunctions, which also provides significant reduction of recombination efficiency. Therefore, the photocatalytic dye degradation efficiency of Pt@CN/20%BMO is more enhanced than those of the pure BMO, CN and even for the CN/BMO composites.

In this work, Pt nanoparticles were successfully decorated the Bi_2MoO_6 (BMO) and $\text{g-C}_3\text{N}_4$ (CN) heterojunctions by a one-step facile hydrothermal method. It is confirmed that the Pt decorated CN and BMO heterojunctions with 20% weight percent of BMO (Pt@CN/20%BMO) with a large specific surface area and the modified band gap present a much higher photocatalytic activity for MB degradation compared to the pure CN and BMO as well as the CN/BMO composites. The decorated Pt nanoparticles on the composites could act as a solid-state electron mediator that plays a significant role to promote electron transfer and suppress the recombination rate of electron-hole pairs, thus improving the photostability. In addition, the observation of the improved absorption intensity in the visible light region for the Pt@CN/20%BMO photocatalyst indicates that the band structure could be effectively altered to enhance the visible light response and charge transformation. As a consequence, the photocatalytic activity could be largely improved by the use of the simply synthetic Pt@CN/20%BMO composites, providing new insights into the future work on the synthesis of green photocatalysts.

Methods

Materials. Bismuth nitrate pentahydrate ($\text{Bi}(\text{NO}_3)_3 \cdot 5\text{H}_2\text{O}$), ammonium molybdate tetrahydrate ($(\text{NH}_4)_6\text{Mo}_7\text{O}_{24} \cdot 4\text{H}_2\text{O}$), potassium tetrachloroplatinate (K_2PtCl_4) and melamine were purchased from Strem Chemicals, INC (USA). Chromium trioxide (CrO_3), sodium oxalate (SO, $\text{Na}_2\text{C}_2\text{O}_4$), 1,4-benzoquinone (BQ) and isopropanol (IPA) supplied from J&K Scientific Ltd., (China) were used throughout this work as electron (e^-), hole (h^+),

superoxide radicals ($\cdot\text{O}_2^-$), and hydroxyl radicals ($\cdot\text{OH}$) scavengers, respectively. The methylene blue (MB) dye was supplied from Sigma Aldrich. Other chemicals such as HNO_3 (0.5 M), NaOH (0.5 M), distilled water, were all of the analytical grades.

Synthesis of g- $\text{C}_3\text{N}_4/\text{Bi}_2\text{MoO}_6/\text{Pt}$ heterojunctions. Melamine was directly heated to prepare the g- C_3N_4 (CN) powders in a semi-closed system by a reported method⁵⁵. Typically, 10 g of melamine in a covered crucible under ambient pressure in air was heated to 520 °C in a muffle furnace at a heating rate of 5 °C/min and then retained for 140 min.

The Bi_2MoO_6 (BMO) microplates were synthesized by a simply hydrothermal process. In detail, 1.00 mmol (0.485 g) of $\text{Bi}(\text{NO}_3)_3 \cdot 5\text{H}_2\text{O}$ and 0.07 mmol (0.088 g) of $(\text{NH}_4)_6\text{Mo}_7\text{O}_{24} \cdot 4\text{H}_2\text{O}$ were dissolved in 40 mL distilled water followed by vigorous stirring for 60 min. After being another sonicated 10 min, the resultant solution was transferred into a 50 mL Teflon-lined stainless-steel autoclave and heated up to 160 °C for overnight with naturally cooling to room temperature. Afterwards, the solid samples were obtained by filtration, which were washed with distilled water by 3 times. The collected powders were further dried at 80 °C in air overnight then annealed in a muffle furnace at 400 °C for 3 h at a heating rate of 5 °C/min.

g- $\text{C}_3\text{N}_4/\text{Bi}_2\text{MoO}_6$ and Pt decorated g- $\text{C}_3\text{N}_4/\text{Bi}_2\text{MoO}_6$ heterojunctions were synthesized by one step facile hydrothermal method. For the g- $\text{C}_3\text{N}_4/\text{Bi}_2\text{MoO}_6$ heterojunctions, 0.485 g of $\text{Bi}(\text{NO}_3)_3 \cdot 5\text{H}_2\text{O}$ and 0.088 g of $(\text{NH}_4)_6\text{Mo}_7\text{O}_{24} \cdot 4\text{H}_2\text{O}$ were firstly dissolved in 40 mL distilled water under stirring for 60 min. Afterwards, different weights of g- C_3N_4 (i.e. 2.7 g, 1.2 g and 0.3 g) were gradually added into the mixed solvent and stirred for another 30 min. The weight percentages of Bi_2MoO_6 in g- $\text{C}_3\text{N}_4/\text{Bi}_2\text{MoO}_6$ composites were 10%, 20% and 50%, denoted as CN/10%BMO, CN/20%BMO and CN/50%BMO in this work. For the preparation of Pt decorated g- $\text{C}_3\text{N}_4/\text{Bi}_2\text{MoO}_6$ heterojunctions, 0.157 mmol (0.065 g) of K_2PtCl_4 was gradually dropped into the pre-prepared mixed solution containing $\text{Bi}(\text{NO}_3)_3 \cdot 5\text{H}_2\text{O}$ and $(\text{NH}_4)_6\text{Mo}_7\text{O}_{24} \cdot 4\text{H}_2\text{O}$ for stirring another 30 min. Then 1.2 g g- C_3N_4 (20%BMO) was added into the solution for vigorous stirring in 30 min. The Pt decorated CN/20%BMO composites was denoted as Pt@CN/20%BMO. After being sonicated for 10 min, the mixed composites were heated, filtrated, dried and annealed as the same procedures of the abovementioned Bi_2MoO_6 preparation (the annealed temperature of Pt decorated heterojunction was at 350 °C with the same heating rate of 5 °C/min).

Characterizations. The SEM (JEOL JSM-820) and TEM (JEOL TEM 2100F FEG) as well as HRTEM equipped with energy-dispersive X-ray spectroscopy (EDS) were employed for characterizing the surface morphology and inner structure of the as-prepared samples. The crystalline phases of the samples were examined by XRD (Rigaku SmartLab) using $\text{Cu K}\alpha$ radiation. XPS measurements were performed on a VG ESCALAB 220i-XL surface analysis system to record the surface atomic distribution of the as-prepared powders. The structural characterization of the samples was collected using FTIR (Thermo Scientific iS50). The UPS (VG ESCALAB 220i-XL) and UV-Vis DRS (PerkinElmer Lambda 750) using BaSO_4 as the reference were employed to characterize the electronic levels and band structures of the as-prepared samples. The specific surface area was recorded by BET on a Micromeritics, ASAP2020 gas sorption analyzer at 77 K. TGA was carried out on a TGA Q50 instrument by heating from 30 to 800 °C at a heating rate of 10 °C/min under nitrogen protection. The UV-Vis spectrometer (PerkinElmer Lambda2S) was employed for measuring the dye absorbance.

Photocatalytic activity. In the photocatalytic experiments, a specific mass of the as-prepared photocatalysts was dispersed in 100 mL of MB solution with 10 ppm concentration (10 mg/L). The MB solution with catalysts was initially stirred for 60 min in darkness to achieve equilibrium adsorption, followed by a direct irradiation under a source of 300 W Xeon simulated solar light lamp with an ultraviolet cut off filter (≥ 420 nm) to provide visible light. Afterwards, 4 mL of the MB solution were taken at different predetermined time intervals and separated in a MIKRO 185 centrifuge at 10000 rpm for 2 min to remove the remaining solid catalysts. Then the samples were recorded by the UV-Vis spectrometer and COD determination with reference to dichromate method (HJ 828–2017 standard). The wavelength of light absorbance λ_{max} of MB solution was at 664 nm^{67,68}. The dye degradation efficiency were evaluated by the following Equation 3⁶⁹:

$$X = (C_0 - C)/C_0 \times 100\% \quad (4)$$

whereas C_0 and C are the initial concentration and the concentration at time t of MB dye, respectively.

References

- Ribeiro, A. R., Nunes, O. C., Pereira, M. F. R. & Silva, A. M. T. An overview on the advanced oxidation processes applied for the treatment of water pollutants defined in the recently launched Directive 2013/39/EU. *Environ. Int.* **75**, 33–51 (2015).
- Jia, Z. *et al.* Attractive *In Situ* Self-Reconstructed Hierarchical Gradient Structure of Metallic Glass for High Efficiency and Remarkable Stability in Catalytic Performance. *Adv. Funct. Mater.* **29**, 1807857 (2019).
- Liang, S. X. *et al.* Compelling Rejuvenated Catalytic Performance in Metallic Glasses. *Adv. Mater.* **30**, 1802764 (2018).
- Wang, J. C. *et al.* Chemically dealloyed Fe-based metallic glass with void channels-like architecture for highly enhanced peroxymonosulfate activation in catalysis. *J. Alloys Compd.* **785**, 642–650 (2019).
- Jia, Z. *et al.* Activation of peroxymonosulfate by Fe78Si9B13 metallic glass: the influence of crystallization. *J. Alloys Compd.* **728**, 525–533 (2017).
- Miao, J., Lin, H. C., Wang, W. M. & Zhang, L. C. Amphoteric composite membranes for nanofiltration prepared from sulfated chitosan crosslinked with hexamethylene diisocyanate. *Chem. Eng. J.* **234**, 132–139 (2013).
- Jia, Z. *et al.* Heterogeneous photo Fenton-like degradation of the cibacron brilliant red 3B-A dye using amorphous Fe78Si9B13 and Fe73.5Si13.5B9Cu1Nb3 alloys: The influence of adsorption. *J. Taiwan Inst. Chem. Eng.* **71**, 128–136 (2017).
- Liang, S. X., Jia, Z., Zhang, W. C., Wang, W. M. & Zhang, L. C. Rapid malachite green degradation using Fe73.5Si13.5B9Cu1Nb3 metallic glass for activation of persulfate under UV-Vis light. *Mater. Des.* **119**, 244–253 (2017).
- Li, X.-F. *et al.* Excellent Performance of Fe78Si9B13 Metallic Glass for Activating Peroxymonosulfate in Degradation of Naphthol Green B. *Metals* **7**, 273 (2017).

10. Vittenet, J. *et al.* Removal of 2,4-dimethylphenol pollutant in water by ozonation catalyzed by SOD, LTA, FAU-X zeolites particles obtained by pseudomorphic transformation (binderless). *Microporous Mesoporous Mater.* **189**, 200–209 (2014).
11. Álvarez, P. M., Beltrán, F. J., Masa, F. J. & Pocostales, J. P. A Comparison between catalytic ozonation and activated carbon adsorption/ozonation processes for wastewater treatment. *Appl. Catal. B: Environ.* **92**, 393–400 (2009).
12. Broseus, R. *et al.* Ozone oxidation of pharmaceuticals, endocrine disruptors and pesticides during drinking water treatment. *Water Res.* **43**, 4707–4717 (2009).
13. Lee, S.-K., Mills, A. & O'Rourke, C. Action spectra in semiconductor photocatalysis. *Chem. Soc. Rev.* **46**, 4877–4894 (2017).
14. Fujishima, A. & Honda, K. Electrochemical Photolysis of Water at a Semiconductor Electrode. *Nature* **238**, 37 (1972).
15. Jia, Z. *et al.* Photocatalytic degradation and absorption kinetics of cibacron brilliant yellow 3G-P by nanosized ZnO catalyst under simulated solar light. *J. Taiwan Inst. Chem. Eng.* **60**, 267–274 (2016).
16. Jia, Z. *et al.* Strong enhancement on dye photocatalytic degradation by ball-milling TiO₂: a study of cationic and anionic dyes. *J. Mater. Sci. Technol.* **33**, 856–863 (2017).
17. Parzinger, E. *et al.* Photocatalytic Stability of Single- and Few-Layer MoS₂. *ACS Nano* **9**, 11302–11309 (2015).
18. Mahler, B., Hoepfner, V., Liao, K. & Ozin, G. A. Colloidal Synthesis of 1T-WS₂ and 2H-WS₂ Nanosheets: Applications for Photocatalytic Hydrogen Evolution. *J. Am. Chem. Soc.* **136**, 14121–14127 (2014).
19. Kim, E. S. *et al.* Fabrication of CaFe₂O₄/TaON Heterojunction Photoanode for Photoelectrochemical Water Oxidation. *J. Am. Chem. Soc.* **135**, 5375–5383 (2013).
20. Li, C. *et al.* Doping effect of phosphate in Bi₂WO₆ and universal improved photocatalytic activity for removing various pollutants in water. *Appl. Catal. B: Environ.* **188**, 39–47 (2016).
21. Chen, J., Shen, S., Wu, P. & Guo, L. Nitrogen-doped CeOx nanoparticles modified graphitic carbon nitride for enhanced photocatalytic hydrogen production. *Green Chem.* **17**, 509–517 (2015).
22. Wu, D. *et al.* Boron doped BiOBr nanosheets with enhanced photocatalytic inactivation of *Escherichia coli*. *Appl. Catal. B: Environ.* **192**, 35–45 (2016).
23. Zhang, Z., Liu, K., Feng, Z., Bao, Y. & Dong, B. Hierarchical Sheet-on-Sheet ZnIn₂S₄/g-C₃N₄ Heterostructure with Highly Efficient Photocatalytic H₂ production Based on Photoinduced Interfacial Charge Transfer. *Sci. Rep.* **6**, 19221 (2016).
24. Cai, J., Huang, J. & Lai, Y. 3D Au-decorated BiMoO₆ nanosheet/TiO₂ nanotube array heterostructure with enhanced UV and visible-light photocatalytic activity. *J. Mater. Chem. A* **5**, 16412–16421 (2017).
25. Niu, M., Cheng, D. & Cao, D. SiH/TiO₂ and GeH/TiO₂ Heterojunctions: Promising TiO₂-based Photocatalysts under Visible Light. *Sci. Rep.* **4**, 4810 (2014).
26. Feng, Y. *et al.* Honeycomb-like ZnO Mesoporous Nanowall Arrays Modified with Ag Nanoparticles for Highly Efficient Photocatalytic Activity. *Sci. Rep.* **7**, 11622 (2017).
27. Liu, X. *et al.* A general nonaqueous sol-gel route to g-C₃N₄-coupling photocatalysts: the case of Z-scheme g-C₃N₄/TiO₂ with enhanced photodegradation toward RhB under visible-light. *Sci. Rep.* **6**, 39531 (2016).
28. Basith, M. A., Ahsan, R., Zarin, I. & Jalil, M. A. Enhanced photocatalytic dye degradation and hydrogen production ability of Bi₂FeO₄-rGO nanocomposite and mechanism insight. *Sci. Rep.* **8**, 11090 (2018).
29. Ji, L., Zhang, Y., Miao, S., Gong, M. & Liu, X. *In situ* synthesis of carbon doped TiO₂ nanotubes with an enhanced photocatalytic performance under UV and visible light. *Carbon* **125**, 544–550 (2017).
30. Shuang, S., Lv, R., Xie, Z. & Zhang, Z. Surface Plasmon Enhanced Photocatalysis of Au/Pt-decorated TiO₂ Nanopillar Arrays. *Sci. Rep.* **6**, 26670 (2016).
31. Zhang, Z. *et al.* Facile one-step synthesis of TiO₂/Ag/SnO₂ ternary heterostructures with enhanced visible light photocatalytic activity. *Sci. Rep.* **8**, 10532 (2018).
32. Sim, L. C., Leong, K. H., Saravanan, P. & Ibrahim, S. Rapid thermal reduced graphene oxide/Pt–TiO₂ nanotube arrays for enhanced visible-light-driven photocatalytic reduction of CO₂. *Appl. Surf. Sci.* **358**, 122–129 (2015).
33. Dong, F. *et al.* Simultaneous Pd²⁺ doping and Pd metal deposition on (BiO)₂CO₃ microspheres for enhanced and stable visible light photocatalysis. *Appl. Catal. A: Gen.* **510**, 161–170 (2016).
34. Hao, Y. *et al.* Controllable self-assembly of a novel Bi₂MoO₆-based hybrid photocatalyst: excellent photocatalytic activity under UV, visible and near-infrared irradiation. *Chem. Commun.* **52**, 6525–6528 (2016).
35. Li, J. *et al.* *In situ* growing Bi₂MoO₆ on g-C₃N₄ nanosheets with enhanced photocatalytic hydrogen evolution and disinfection of bacteria under visible light irradiation. *J. Hazard. Mater.* **321**, 183–192 (2017).
36. Lin, X. *et al.* SiO₂/Bi₂MoO₆ nanocomposites with high photocatalytic activity under visible light irradiation. *Mater. Res. Bull.* **63**, 72–79 (2015).
37. Miao, J., Jia, Z., Lu, H.-B., Habibi, D. & Zhang, L.-C. Heterogeneous photocatalytic degradation of mordant black 11 with ZnO nanoparticles under UV-Vis light. *J. Taiwan Inst. Chem. Eng.* **45**, 1636–1641 (2014).
38. Li, H., Li, W., Wang, F., Liu, X. & Ren, C. Fabrication of two lanthanides co-doped Bi₂MoO₆ photocatalyst: Selection, design and mechanism of Ln¹/Ln² redox couple for enhancing photocatalytic activity. *Appl. Catal. B: Environ.* **217**, 378–387 (2017).
39. Wu, X. *et al.* Improving the Photo-oxidative Performance of Bi₂MoO₆ by Harnessing the Synergy between Spatial Charge Separation and Rational Co-catalyst Deposition. *ACS Appl. Mater. Interfaces* **10**, 9342–9352 (2018).
40. Li, H., Hu, T., Zhang, R., Liu, J. & Hou, W. Preparation of solid-state Z-scheme Bi₂MoO₆/MO (MCu, Co₃/4, or Ni) heterojunctions with internal electric field-improved performance in photocatalysis. *Appl. Catal. B: Environ.* **188**, 313–323 (2016).
41. Gao, J. *et al.* Facile Synthesis of Heterostructured WS₂/Bi₂MoO₆ as High-Performance Visible-Light-Driven Photocatalysts. *Nanoscale Res. Lett.* **12**, 377 (2017).
42. Liang, Q. *et al.* High performance visible-light driven photocatalysts of Bi₂MoO₆-g-C₃N₄ with controllable solvothermal fabrication. *J. Photochem. Photobiol., A* **332**, 357–363 (2017).
43. Hu, C., Hung, W.-Z., Wang, M.-S. & Lu, P.-J. Phosphorus and sulfur codoped g-C₃N₄ as an efficient metal-free photocatalyst. *Carbon* **127**, 374–383 (2018).
44. Lu, X., Wang, Q. & Cui, D. Preparation and Photocatalytic Properties of g-C₃N₄/TiO₂ Hybrid Composite. *J. Mater. Sci. Technol.* **26**, 925–930 (2010).
45. Sun, J.-X. *et al.* Fabrication of composite photocatalyst g-C₃N₄-ZnO and enhancement of photocatalytic activity under visible light. *Dalton Trans.* **41**, 6756–6763 (2012).
46. Li, G., Yang, N., Wang, W. & Zhang, W. F. Synthesis, Photophysical and Photocatalytic Properties of N-Doped Sodium Niobate Sensitized by Carbon Nitride. *J. Phys. Chem. C* **113**, 14829–14833 (2009).
47. Ge, L., Han, C. & Liu, J. Novel visible light-induced g-C₃N₄/Bi₂WO₆ composite photocatalysts for efficient degradation of methyl orange. *Appl. Catal. B: Environ.* **108–109**, 100–107 (2011).
48. Yan, S. C., Lv, S. B., Li, Z. S. & Zou, Z. G. Organic-inorganic composite photocatalyst of g-C₃N₄ and TaON with improved visible light photocatalytic activities. *Dalton Trans.* **39**, 1488–1491 (2010).
49. Samanta, S., Martha, S. & Parida, K. Facile Synthesis of Au/g-C₃N₄ Nanocomposites: An Inorganic/Organic Hybrid Plasmonic Photocatalyst with Enhanced Hydrogen Gas Evolution Under Visible-Light Irradiation. *ChemCatChem* **6**, 1453–1462 (2014).
50. Liang, S. *et al.* Au and Pt co-loaded g-C₃N₄ nanosheets for enhanced photocatalytic hydrogen production under visible light irradiation. *Appl. Surf. Sci.* **358**, 304–312 (2015).
51. Li, Z., Wang, J., Zhu, K., Ma, F. & Meng, A. Ag/g-C₃N₄ composite nanosheets: Synthesis and enhanced visible photocatalytic activities. *Mater. Lett.* **145**, 167–170 (2015).

52. Elavarasan, S. *et al.* An efficient mesoporous carbon nitride (g-C₃N₄) functionalized Pd catalyst for carbon-carbon bond formation reactions. *RSC Adv.* **6**, 49376–49386 (2016).
53. Zhu, Y.-P., Ren, T.-Z. & Yuan, Z.-Y. Mesoporous Phosphorus-Doped g-C₃N₄ Nanostructured Flowers with Superior Photocatalytic Hydrogen Evolution Performance. *ACS Appl. Mater. Interfaces* **7**, 16850–16856 (2015).
54. Guo, F., Shi, W., Zhu, C., Li, H. & Kang, Z. CoO and g-C₃N₄ complement each other for highly efficient overall water splitting under visible light. *Appl. Catal. B: Environ.* **226**, 412–420 (2018).
55. Li, H. *et al.* Synthesis and characterization of g-C₃N₄/Bi₂MoO₆ heterojunctions with enhanced visible light photocatalytic activity. *Appl. Catal. B: Environ.* **160–161**, 89–97 (2014).
56. Xu, Y.-S. & Zhang, W.-D. Monodispersed Ag₃PO₄ nanocrystals loaded on the surface of spherical Bi₂MoO₆ with enhanced photocatalytic performance. *Dalton Trans.* **42**, 1094–1101 (2013).
57. Zhang, M. *et al.* Hierarchical heterostructures of Bi₂MoO₆ on carbon nanofibers: controllable solvothermal fabrication and enhanced visible photocatalytic properties. *J. Mater. Chem.* **22**, 577–584 (2012).
58. Yang, Y. *et al.* Massive Ti³⁺ self-doped by the injected electrons from external Pt and the efficient photocatalytic hydrogen production under visible-light. *Appl. Catal. B: Environ.* **218**, 751–757 (2017).
59. Yan, T. *et al.* Facile fabrication of heterostructured g-C₃N₄/Bi₂MoO₆ microspheres with highly efficient activity under visible light irradiation. *Dalton Trans.* **44**, 1601–1611 (2015).
60. Tian, J., Hao, P., Wei, N., Cui, H. & Liu, H. 3D Bi₂MoO₆ Nanosheet/TiO₂ Nanobelt Heterostructure: Enhanced Photocatalytic Activities and Photoelectrochemistry Performance. *ACS Catal.* **5**, 4530–4536 (2015).
61. Liu, J. *et al.* Metal-free efficient photocatalyst for stable visible water splitting via a two-electron pathway. *Science* **347**, 970–974 (2015).
62. Li, T. *et al.* Synthesis of g-C₃N₄/SmVO₄ composite photocatalyst with improved visible light photocatalytic activities in RhB degradation. *Appl. Catal. B: Environ.* **129**, 255–263 (2013).
63. Di, L., Yang, H., Xian, T. & Chen, X. Enhanced Photocatalytic Degradation Activity of BiFeO₃ Microspheres by Decoration with g-C₃N₄ Nanoparticles. *Mater. Res.* **21** (2018).
64. Jia, Z. *et al.* Disordered Atomic Packing Structure of Metallic Glass: Toward Ultrafast Hydroxyl Radicals Production Rate and Strong Electron Transfer Ability in Catalytic Performance. *Adv. Funct. Mater.* **27**, 1702258 (2017).
65. Zhang, T. *et al.* Photooxidative N-demethylation of methylene blue in aqueous TiO₂ dispersions under UV irradiation. *J. Photochem. Photobiol. A* **140**, 163–172 (2001).
66. Zhu, H. *et al.* Construction of Z-scheme type CdS–Au–TiO₂ hollow nanorod arrays with enhanced photocatalytic activity. *Appl. Catal. B: Environ.* **90**, 463–469 (2009).
67. Li, J., Yuan, H. & Zhu, Z. Photoelectrochemical performance of g-C₃N₄/Au/BiPO₄ Z-scheme composites to improve the mineralization property under solar light. *RSC Adv.* **6**, 70563–70572 (2016).
68. Zhu, C. *et al.* Fabrication of Z-scheme Ag₃PO₄/MoS₂ composites with enhanced photocatalytic activity and stability for organic pollutant degradation. *Appl. Surf. Sci.* **377**, 99–108 (2016).
69. Li, H., Yu, H., Quan, X., Chen, S. & Zhang, Y. Uncovering the Key Role of the Fermi Level of the Electron Mediator in a Z-Scheme Photocatalyst by Detecting the Charge Transfer Process of WO₃-metal-gC₃N₄ (Metal = Cu, Ag, Au). *ACS Appl. Mater. Interfaces* **8**, 2111–2119 (2016).
70. Wei, N. *et al.* Highly efficient photocatalytic activity of Ag₃PO₄/Ag/ZnS(en)0.5 photocatalysts through Z-scheme photocatalytic mechanism. *RSC Adv.* **7**, 18392–18399 (2017).
71. Gong, Y., Quan, X., Yu, H. & Chen, S. Synthesis of Z-scheme Ag₂CrO₄/Ag/g-C₃N₄ composite with enhanced visible-light photocatalytic activity for 2,4-dichlorophenol degradation. *Appl. Catal. B: Environ.* **219**, 439–449 (2017).
72. Li, Q. *et al.* Z-Scheme BiOCl–Au–CdS Heterostructure with Enhanced Sunlight-Driven Photocatalytic Activity in Degrading Water Dyes and Antibiotics. *ACS Sustain. Chem. Eng.* **5**, 6958–6968 (2017).
73. Ma, D., Wu, J., Gao, M., Xin, Y. & Chai, C. Enhanced debromination and degradation of 2,4-dibromophenol by an Z-scheme Bi₂MoO₆/CNTs/g-C₃N₄ visible light photocatalyst. *Chem. Eng. J.* **316**, 461–470 (2017).
74. Liang, S. X. *et al.* Ultrafast activation efficiency of three peroxides by Fe₇₈Si₉B₁₃ metallic glass under photo-enhanced oxidative degradation: a comparative study. *Appl. Catal. B: Environ.* **221**, 108–118 (2018).
75. Jia, Z. *et al.* Surface aging behaviour of Fe-based amorphous alloys as catalysts during heterogeneous photo-Fenton-like process for water treatment. *Appl. Catal. B: Environ.* **204**, 537–547 (2017).
76. Jia, Z. *et al.* Ultra-sustainable Fe₇₈Si₉B₁₃ metallic glass as a catalyst for activation of persulfate on methylene blue degradation under UV-Vis light. *Sci. Rep.* **6**, 38520 (2016).
77. Jia, Z., Zhang, W. C., Wang, W. M., Habibi, D. & Zhang, L. C. Amorphous Fe₇₈Si₉B₁₃ alloy: An efficient and reusable photo-enhanced Fenton-like catalyst in degradation of cibacron brilliant red 3B-A dye under UV-vis light. *Appl. Catal. B: Environ.* **192**, 46–56 (2016).
78. Luo, J. *et al.* Synthesis and characterization of Z-scheme In₂S₃/Ag₂CrO₄ composites with an enhanced visible-light photocatalytic performance. *New J. Chem.* **41**, 845–856 (2017).

Acknowledgements

This work was supported by the National Key R&D Program of China (Project No. 2017YFA0204403), the Major Program of National Natural Science Foundation of China: NSFC 51590892, the RGC Hong Kong General Research Fund (grant number CityU 11247516), and Hong Kong Innovation and Technology Commission via the Hong Kong Branch of National Precious Metals Material Engineering Research Center (Grant No. 9448003). The authors appreciate Mr. Muqing Li and Mr. Dong Shen for the UV-DRS and UPS measurements.

Author Contributions

Z.J. and J.L. conceived the experiments and wrote the manuscript. Z.J., F.L. and S.Z. conducted the experiments. Z.J., F.L., L.C.Z., S.X.L., Y.Y.L. and J.L. analyzed the data. All authors reviewed the manuscript.

Additional Information

Supplementary information accompanies this paper at <https://doi.org/10.1038/s41598-019-42973-6>.

Competing Interests: The authors declare no competing interests.

Publisher's note: Springer Nature remains neutral with regard to jurisdictional claims in published maps and institutional affiliations.



Open Access This article is licensed under a Creative Commons Attribution 4.0 International License, which permits use, sharing, adaptation, distribution and reproduction in any medium or format, as long as you give appropriate credit to the original author(s) and the source, provide a link to the Creative Commons license, and indicate if changes were made. The images or other third party material in this article are included in the article's Creative Commons license, unless indicated otherwise in a credit line to the material. If material is not included in the article's Creative Commons license and your intended use is not permitted by statutory regulation or exceeds the permitted use, you will need to obtain permission directly from the copyright holder. To view a copy of this license, visit <http://creativecommons.org/licenses/by/4.0/>.

© The Author(s) 2019